

Three-Dimensional Modeling of Multiple Automated Equilibrium Tension Lysimeters to Measure Vadose Zone Fluxes

Thomas Wöhling,* Niels Schütze, Ben Heinrich, Jirka Šimůnek, and Gregory F. Barkle

Using numerical simulation, we analyzed a novel vadose zone sampling system installed in a vadose zone of volcanic origin in the Lake Taupo catchment, New Zealand. The system comprises 15 Automated Equilibrium Tension Lysimeters (AETLs) installed at five depths. The vacuum in each individual lysimeter is controlled to match the pressure head measured at a reference location in the undisturbed vadose zone. The three-dimensional numerical flow model HYDRUS-3D was used to investigate the impact of flow impediment and shadow effects caused by the installation and operation of the AETLs. The analysis was conducted for steady-state conditions in homogeneous sand, loam, and ignimbrite, as well as in the layered materials present at the experimental site. The hydraulic properties of the different layers were estimated using one-dimensional inverse modeling and global optimization techniques. Horizontal, vertical, and radial two-dimensional sections through the model domain were analyzed for divergence from steady-state conditions. The results suggest that the sampling efficiency of the AETLs is relatively large and the errors caused by the setup and operation of the vadose zone sampler are relatively small. We further utilized a transient HYDRUS-3D model of the vadose zone sampler to simulate transient tensiometric pressure heads using field data. The simulations for the various depths compared favorably with both the measured pressure heads and the simulations of the one-dimensional model. In contrast, the simulated cumulative water fluxes during the evaluation period were larger than the measurements of the corresponding AETLs. These findings highlight the importance of an adequate model structure and information content of the calibration data for the accurate prediction of vadose zone water fluxes.

ABBREVIATIONS: AETL, automated equilibrium tension lysimeter; FE, finite element; MVG, Mualem-van Genuchten model.

TO DATE, the development of direct methods to measure vadose zone water and contaminant fluxes remains a challenge. In the past, researchers have used in situ sampling techniques such as porous suction samplers, zero-tension lysimeters, wick samplers, and tension plate lysimeters (Dorrance et al., 1991; Wilson et al., 1995; Brye et al., 1999; Weihermüller et al., 2005; Masarik et al., 2004; Kosugi and Katsuyama, 2004; Mertens et al., 2007; and others). Tension plate lysimeters made of relatively large porous ceramic or sintered stainless steel have recently gained popularity; however, the strategy for setting the tension in the lysimeters is still debated. Zero-tension lysimeters sample only when a

saturated zone develops above the plate and the hydraulic head in the soil matrix is large enough to overcome the resistance of the plate material. Constant-tension lysimeters are sampling under unsaturated conditions but only a portion of the pore space is sampled, the range of which depends on the vadose zone material characteristics and the tension level applied. Both methods create artifacts in the measurements.

To overcome this problem and to accurately measure vadose zone water and contaminant fluxes, we advocate a method similar to that proposed by Masarik et al. (2004) where the tension applied to the lysimeter at a given time is controlled by the surrounding “undisturbed” soil pressure head. A novel vadose sampling system has recently been developed and installed to measure vadose zone fluxes at the Spydia experimental site in New Zealand (Wöhling et al., 2008). It consists of 15 AETLs made of porous stainless steel plates, which were installed at five depths around a central access caisson. With the unique setup of the sampling system, fluxes of water and contaminants can be traced from the soil surface to the bottom of the root zone and through different depths in the vadose zone down to the permanently saturated zone.

A two-dimensional numerical study was performed before the installation of the vadose zone sampler to determine the design parameters of the AETLs and their best location to minimize the effects on the sampling efficiency of the dry zones developing below the lysimeters (Mertens et al., 2005). The study was conducted for a vertical plane using a two-dimensional model and thus ignoring the three-dimensional nature of the flow system. The soil hydraulic parameters used were based on early exploratory

T. Wöhling, Lincoln Environmental Research, Lincoln Ventures Ltd., Ruakura Research Centre, Hamilton 3240, New Zealand; N. Schütze, Institute for Hydrology and Meteorology, Dresden Univ. of Technology, Würzburger Str. 46, 01187 Dresden, Germany; B. Heinrich, Soil and Groundwater Lab., Tiergartenstr. 48, 01219 Dresden, Germany; J. Šimůnek, Dep. of Environmental Sciences, Univ. of California, Riverside, CA; and G.F. Barkle, Aqualinc Research Ltd, P.O. Box 14-041, Enderley, Hamilton, New Zealand. *Corresponding author (woehling@lvrham.lincoln.ac.nz).

Vadose Zone J. 8:1051–1063
doi:10.2136/vzj2009.0040
Received 2 Apr. 2009.
Published online 27 Oct. 2009.

© Soil Science Society of America
677 S. Segoe Rd. Madison, WI 53711 USA
All rights reserved. No part of this periodical may be reproduced or transmitted in any form or by any means, electronic or mechanical, including photocopying, recording, or any information storage and retrieval system, without permission in writing from the publisher.

data. More recently we have gained a better understanding of the degree of detail needed to describe well-draining, coarse-textured, vadose zone materials at the Spydia site.

In this study, we applied a three-dimensional model to the Spydia vadose zone sampler using the HYDRUS-3D model (Šimůnek et al., 2006). This enabled us for the first time to study the three-dimensional flow divergence (“dry zones”) caused by the presence of the AETLs at the Spydia site and their impact on the accuracy of the flux measurements. Since the complex input function of the transient model impedes the understanding of the resulting transient flow divergence patterns, we first conducted a comprehensive steady-state flow analysis. This enabled us to investigate qualitatively and quantitatively the potential impact of soil type and stratification on the three-dimensional extent of the dry zones for the proposed design of the vadose zone sampler. The analysis yielded valuable insights about the transferability of the sampler design to other field sites. We conducted transient, three-dimensional model runs for the heterogeneous Spydia vadose zone and compared the model simulations with field measurements of tensiometric pressure head and water flux. The aims of this study are summarized as follows:

1. Analyze the three-dimensional flow divergence patterns caused by the presence of the AETLs for steady-state flow and investigate their sensitivity to soil type and vadose zone stratification
2. Show that AETLs can accurately measure fluxes in different vadose zone materials and under different boundary flux scenarios
3. Infer parameters for the three-dimensional flow model from one-dimensional inverse modeling using field data and global optimization techniques
4. Evaluate the transient, heterogeneous, three-dimensional Spydia model using independent field measured data.

Materials and Methods

Experimental Setup and Field Data

The Spydia experimental site is located in the Tutaeuaua sub-catchment (Landcorp’s Waihora Station, 175.79977 E, 38.61423 S) north of Lake Taupo, New Zealand, on a sheep and beef farm under pastoral land use. Installed in 2005, the main purpose of the Spydia experimental site is the investigation of water and solute movement through the vadose zone and the transformation processes occurring in the profile. The vadose zone materials at Spydia encompass a young volcanic soil (0–1.6-m depth) that belongs to the Oruanui loamy sand series (Podzolic Orthic Pumice soil) developed on the underlying unwelded Taupo ignimbrite (1.6–4.2 m). Two older buried paleosol layers (4.2–5.8-m depth) and unwelded Oruanui ignimbrite follow below.

The Spydia vadose zone sampling system comprises measurements at 15 different locations (sites) in the vadose zone profile, namely at the 0.4-, 1.0-, 2.6-, 4.2-, and 5.1-m depths and at three locations at each depth. At each site, tensiometric pressure head (tensiometer type T4e, UMS GmbH, München, Germany; accuracy ± 0.05 m) is measured in conjunction with water and contaminant fluxes. The fluxes have been measured since January 2008 using AETLs made of porous sintered stainless steel of 1-mm thickness. To sample a representative portion of the vadose zone, the lysimeters have a relatively large active surface area of 0.20 m^2 and a rectangular shape (outer dimensions 0.25 by 0.9 m). The porous sampling plates are separated vertically by 0.5 m from the dry zones that occur under the AETLs, as discussed by Mertens et al. (2005). For undisturbed measurements in the profile, the lysimeters and tensiometers are installed from a cylindrical access caisson (diameter 2.3 m, depth 7 m). The 15 AETLs are installed horizontally and radiate from the center point of the caisson plane at spacings of 24° . Figure 1a shows a schematic of the access caisson and the alignment of the AETLs.

To minimize boundary effects at the caisson wall and provide sufficient spacing, the lysimeters were extended 0.45 m into the undisturbed vadose zone and spacer lysimeters were put in

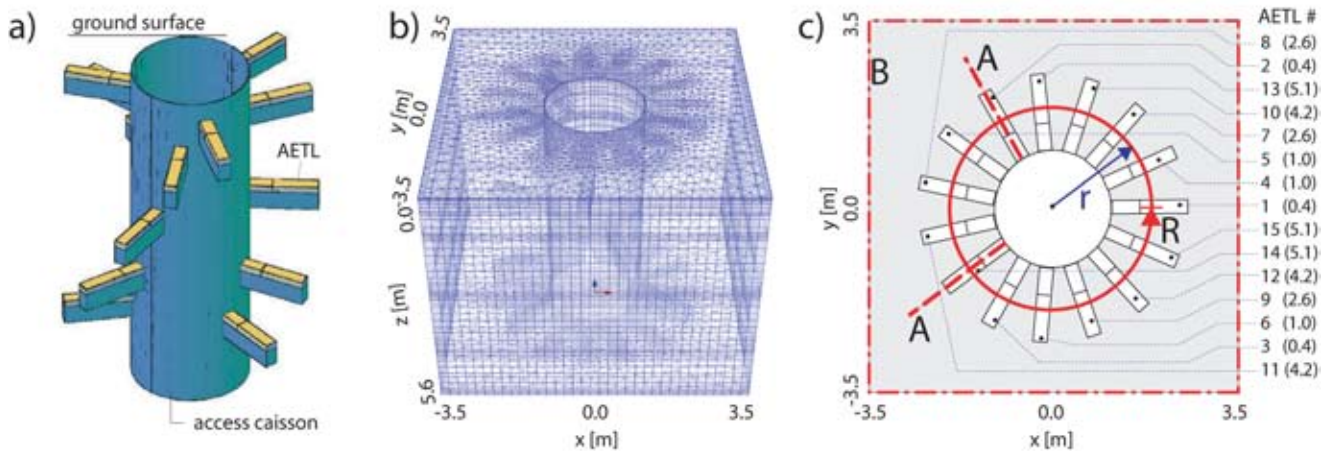


FIG. 1. A three-dimensional model of the Spydia experimental site: (a) the access caisson and the location of the automated equilibrium tension lysimeters (AETLs); (b) the three-dimensional calculation domain of the steady-state model; and (c) a plane view of the domain indicating the AETLs, their numbering (installation depths in parentheses), and the location of cross-sections for interpreting the results. The cross-sections used are vertical cross-sections through the individual AETLs (A), horizontal sections through the x-y plane (B), and vertical cross-sections along the circumference of a circle with radius r , centered in the center of the access caisson (R).

place. The pressure applied to each of the lysimeters is continuously controlled by a FieldPoint cFP2010 controller (National Instruments, Austin, TX) to match the tensiometric pressure head in the adjacent vadose zone materials. These control tensions were measured at the same depth as the AETLs with a horizontal separation distance of 0.6 m from the center point of the AETLs. The leachate from the lysimeters is collected in stainless steel vessels that are weighed by load cells (Tedeo-Huntleigh 1130, Vishay Intertechnology, Malvern, PA; accuracy class C6). All measurements, including the weight of the leachate vessels, are taken by the cFP2010 controller at 15-min intervals.

Daily values of potential evaporation were calculated by the Penman–Monteith equation (Allen et al., 1998) using data from the nearby Waihora meteorological station (500-m distance). Precipitation was measured on site using a 0.2-mm bucket gauge and upscaled to hourly values for use in our calculations. More details of the Spydia experimental data and the setup of the experiment can be found in Wöhling et al. (2008) and is therefore not repeated here.

Model Setup

Governing Flow Equations

We used the HYDRUS-3D model (Šimůnek et al., 2006) to simulate water flow at the Spydia vadose zone sampler. The HYDRUS-3D code utilizes the Galerkin finite element method based on the mass-conservative, iterative scheme proposed by Celia et al. (1990). The model solves a modified form of the three-dimensional Richards equation. Considering isothermal uniform Darcian flow in a rigid isotropic porous medium, the governing flow equation is

$$\frac{\partial \theta}{\partial t} = \frac{\partial}{\partial x} \left[K(h) \frac{\partial h}{\partial x} \right] + \frac{\partial}{\partial y} \left[K(h) \frac{\partial h}{\partial y} \right] + \frac{\partial}{\partial z} \left[K(h) \left[\frac{\partial h}{\partial z} + 1 \right] \right] - S \quad [1]$$

where θ is the volumetric water content [$L^3 L^{-3}$], t represents time [T], x , y , and z are the spatial coordinates [L], h denotes the pressure head [L], S is a sink term representing processes such as plant water uptake [$L^3 L^{-3} T^{-1}$], and K is the unsaturated hydraulic conductivity function [$L T^{-1}$] given by

$$K(h, x, y, z) = K_s(x, y, z) K_r(h, x, y, z) \quad [2]$$

where K_r is the relative hydraulic conductivity and K_s is the saturated hydraulic conductivity [$L T^{-1}$].

We described the highly nonlinear soil water retention, $\theta(h)$, and hydraulic conductivity, $K(h)$, functions in Eq. [1] by using the Mualem–van Genuchten model (MVG; van Genuchten, 1980):

$$K(S_e) = K_s S_e^l \left[1 - (1 - S_e^{1/m})^m \right]^2 \quad [3]$$

$$S_e = \frac{\theta - \theta_r}{\theta_s - \theta_r} = \begin{cases} \theta_r + \frac{1}{[1 + |\alpha h|^n]^m} & h < h_s \\ 1 & h \geq h_s \end{cases} \quad [4]$$

where S_e is the effective water content, θ_r and θ_s denote the residual and saturated water content, respectively [$L^3 L^{-3}$], α [L^{-1}]

and n (dimensionless) are parameters that define the shape of the water retention function, l is the pore-connectivity parameter of Mualem (1976), and $h_s = -0.02$ m is the assumed air-entry value. In this study, we further assumed that $m = 1 - 1/n$ and $n > 1$. We showed in a previous study (Wöhling and Vrugt, 2008) that model ensemble forecasting is preferred to single model forecasts. We also showed, however, that the MVG model performed well compared with other ensemble members for pressure head forecasting at the Spydia site. Therefore (and to keep the analysis clear), we utilized only the MVG in this study.

We set up the three-dimensional Spydia model for two different flow conditions. We first built a steady-state flow model to analyze, for four different vadose zone materials, the impact of flow impediment and shadow effects caused by the AETLs and their operation. Then we set up a transient-flow model for the Spydia site and compared it with field observations. The steady-state and transient models have different flow domains and calculation meshes, as well as different boundary and initial conditions, which are described below.

Steady-State Flow Model

The steady-state Spydia model was embedded in a rectangular calculation domain of 7.0 by 7.0 by 5.6 m. These dimensions appeared to be large enough to not influence the simulated AETL fluxes and the accompanying shadow effects on the one hand and small enough to obtain the required discretization of the calculation mesh on the other hand. The Spydia vadose zone sampler embedded in the domain consists of the central access caisson and the 15 AETLs, which extend from the caisson into the vadose zone. For both the steady-state and the transient models, we followed a sequence of four steps to build the geometry of the model domain and to create the calculation mesh of finite elements (FEs):

1. The base surface of the model domain was created, which included the 15 AETLs as individual objects (surfaces).
2. All elements of the base surface were extruded to the model depth. Subsequently, the model sublayers and FE mesh layers were defined.
3. The mesh density was refined in the vicinity of the AETLs and an intermediate FE mesh was generated.
4. The FE mesh intersections corresponding to the locations of the AETLs were removed and the final FE calculation mesh was generated.

Figure 1b shows the final calculation mesh of the steady-state model. It consisted of 126,360 calculation nodes and 232,070 three-dimensional elements in 57 mesh layers. More detailed information about the creation of the calculation mesh used here can be obtained from the corresponding author.

The initial and boundary conditions used to solve Eq. [1] for the steady-state model are:

$$h(x, y, z, t) = h_i(z) \quad \text{for } t = 0 \quad [5]$$

$$-K \left(\frac{\partial h}{\partial z} + 1 \right) = q_0 \quad \text{at } z = 0 \quad [6]$$

$$K \left(\frac{\partial h}{\partial z} + 1 \right) = q_0 \quad \text{at } (x, y, z) = (\mathbf{x}, \mathbf{y}, z) \quad [7]$$

$$\frac{\partial h}{\partial z} = 1 \quad \text{at } z = L \quad [8]$$

where $h_1(z)$ is the initial pressure head and q_0 is a specified flux [$L^3 L^{-2} T^{-1}$]. The lateral boundaries of the model domain are defined by no-flow boundary conditions ($\partial h/\partial z = 0$). Based on the range of annual recharge derived from water balance calculations for the Spydia site, we investigated a “dry” and a “wet” case with $q_0 = 0.001$ and $0.003 \text{ m}^3 \text{ m}^{-1} \text{ d}^{-1}$, respectively. For readability, we will use the flux units of millimeters per day. Equation [6] describes the constant water flux entering the calculation domain at the upper boundary and Eq. [7] specifies the rate of water leaving the domain by the operation of the AETLs, where $(\mathbf{x}, \mathbf{y}, \mathbf{z})$ denote the vectors of the spatial coordinates associated with the 15 porous lysimeter plates of the AETLs. Equation [8] describes a unit vertical hydraulic gradient that is assigned to the bottom boundary and is associated with free-drainage conditions. The sink term, S in Eq. [1], is set to zero for the steady-state model, i.e., no plant water uptake is considered.

To investigate the sensitivity of the water flow at the Spydia vadose zone sampler to the hydraulic properties of different vadose zone materials, the HYDRUS-3D model was set up for three hypothetical homogeneous materials and the layered Spydia vadose zone. The homogeneous materials included a coarse-textured sand, a fine-textured loam, and ignimbrite material as described in Mertens et al. (2005). Table 1 lists the MVG soil hydraulic parameters for these materials. The layered Spydia vadose zone encompasses various horizons with different hydraulic properties, as described in Wöhling et al. (2008). These horizons were described in our model by five layers. The first three layers represent the Ap, B, and C horizons of the modern soil, respectively, whereas the fourth and fifth layers represent the Taupo ignimbrite and the two paleosol layers, respectively. The soil hydraulic parameters of the different layers were obtained by inverse modeling techniques as described below. The parameters of the calibrated model and the depths of the different layers are listed in Table 1.

The steady-state HYDRUS-3D model runs for the sand, loam, Ignimbrite, and Spydia vadose zone materials are subsequently referred to as the SSa, SLo, SIg, and SSp runs. We further distinguish between the “dry” and the “wet” cases (i.e., the different boundary flux values) with superscripts (d) and (w), respectively.

By definition, the state variables in a steady-state model are constant with time. Since the steady-state pressure head for

the individual runs were unknown a priori, however, we started from an initial pressure head $h_1(z)$ and ran the model for a simulation time of 500 d, by which time steady-state conditions were obtained for all model runs. The runs were subsequently analyzed for differences between the pressure head in the undisturbed material and at the reference locations. We investigated the pressure head and flow velocity divergence from steady-state conditions in the three-dimensional model domain and visualized important results at different two-dimensional cross-sections through the three-dimensional model domain. The locations of the cross-sections are illustrated in Fig. 1c. We analyzed (i) vertical cross-sections through the 15 individual AETLs (A in Fig. 1c); (ii) horizontal sections through the x - y plane (B in Fig. 1c) at the 0.4-, 1.0-, 2.6-, 4.2-, and 5.1-m depths (top of the AETLs); and (iii) vertical cross-sections along the circumference of a circle with radius r , centered in the center of the access caisson (R in Fig. 1c). This analysis was facilitated by interpolating the nodal HYDRUS-3D outputs to a regular visualization mesh created in Matlab (MathWorks, Natick, MA). Note that, for visualization, the vector volume data of flow velocity, \mathbf{v} , was transformed into scalar volume data calculating the magnitude of \mathbf{v} .

The simulation results were analyzed for divergence of pressure head and flow velocity from undisturbed flow conditions. We further defined the sampling efficiency of a particular AETL by

$$E_i = 1 - \frac{v_u - v_{c,i}}{v_u} = 1 - \frac{\Delta v_{c,i}}{v_u} \quad [9]$$

where v_u is the undisturbed flow velocity (i.e., 1 or 3 mm d⁻¹) and $\Delta v_{c,i} = v_u - v_{c,i}$ is the flow velocity deviation at the location of the control tensiometers at AETL i ($i = 1, \dots, 15$). Thus, E is a measure describing the effects of the simulated flow velocity deviations on the control of the AETLs. A value of $E = 1$ is obtained when the flow at the AETL is undisturbed, i.e., when $v_{c,i} = v_u$. In our analysis we report on the minimum and mean sampling efficiency, E_{\min} and \bar{E} , respectively, which were calculated for the set of 15 AETLs. The sampling efficiency under field conditions is affected by a number of other characteristics such as the local variability of soil hydraulic properties; however, that discussion is beyond the scope of this study.

Transient-Flow Model

Initial tests with the calculation mesh shown in Fig. 1b revealed that the spatial discretization of the steady-state model FE mesh was too coarse to ensure numerical stability and the required accuracy of the simulations of the transient model; however, increasing the already large number of calculation nodes

TABLE 1. Soil hydraulic parameters† of the homogeneous vadose zones and the heterogeneous Spydia vadose zone.

Material	Depth	θ_r	θ_s	α	n	K_s	l
	m	m ³ m ⁻³		m ⁻¹		m s ⁻¹	
Sand	0–5.6	0.05	0.43	14.50	2.68	8.25×10^{-5}	0.50
Ignimbrite	0–5.6	0.00	0.67	7.01	1.43	2.84×10^{-5}	0.50
Loam	0–5.6	0.08	0.43	3.60	1.56	2.89×10^{-6}	0.50
Spydia Ap	0–0.1	0.00	0.62	1.40	1.12	4.35×10^{-4}	-1.92
Spydia B	0.1–0.7	0.00	0.30	6.77	1.95	5.66×10^{-4}	2.98
Spydia C	0.7–2.2	0.00	0.63	12.34	1.21	8.96×10^{-6}	-0.37
Spydia Taupo ignimbrite	2.2–4.2	0.00	0.61	14.85	1.44	8.56×10^{-5}	0.27
Spydia paleosol	4.2–5.6	0.00	0.51	6.42	7.03	3.21×10^{-4}	-1.33

† θ_r and θ_s , residual and saturated water contents, respectively; α and n , shape parameters; K_s , saturated hydraulic conductivity; l , pore-connectivity parameter.

and layers in the mesh was impractical. To resolve the problem, we used the fact that the AETLs are aligned at three geometrically identical sectors around the Spydia caisson. Assuming no lateral flow between the three sectors, we set up the calculation domain for a one-third circular sector extruded to a depth of 5.1 m. This reduced the dimensions of the calculation domain significantly. The area of the x - y plane of the transient model calculation domain is 12.54 m³, compared with 37.62 m³ for the steady-state model. Figure 2a shows the final calculation mesh of the transient model. The FE mesh consisted of 171,543 calculation nodes and 325,814 three-dimensional elements in 130 mesh layers. We used the methodology described above to create the FE mesh.

The boundary conditions used to solve Eq. [1] for the transient model are shown in Fig. 2b and are defined as follows:

$$-K \left(\frac{\partial h}{\partial z} + 1 \right) = q(t) \text{ at } z = 0 \text{ for } h_A \leq h \leq h_s$$

$$h(x, y, 0, t) = h_A \quad \text{for } h < h_A \quad [10]$$

$$h(x, y, 0, t) = h_s \quad \text{for } h > h_s$$

$$h(x, y, z, t) = h_L(t) \text{ at } z = L \quad [11]$$

$$h(x, y, z, t) = h_d(t) \text{ at } (x, y, z) = (\mathbf{x}, \mathbf{y}, \mathbf{z})_d \quad [12]$$

for $d = 1, 2, \dots, 5$

where $q(t)$ is the net infiltration rate (i.e., precipitation minus evaporation) and h_A and h_s are the minimum and maximum pressure head allowed at the soil surface. Equation [10] describes the atmospheric boundary condition at the soil-air interface (Šimůnek et al., 2006). This boundary is indicated by the green boundary nodes in Fig. 2b. It switches between a prescribed flux condition and a prescribed head condition, depending on the prevailing transient pressure head conditions near the surface. In our study, we assumed the limits of $h_A = -200$ m and $h_s = -0.02$ m. The bottom boundary condition is described by Eq. [11], where $h_L(t)$ is the prescribed pressure head (observed) at the bottom domain boundary $L = -5.1$ m (blue mesh nodes in Fig. 2b). Equation [12] specifies the boundary condition associated with the control of the AETLs, where $h_d(t)$ denotes the averaged pressure heads for each of the five depths ($d = 1, 2, 3, 4, 5$ corresponds to the 0.4-, 1.0-, 2.6-, 4.2-, and 5.1-m depths, respectively). The vectors $(\mathbf{x}, \mathbf{y}, \mathbf{z})_d$ contain the spatial coordinates of the lysimeter plate at each depth as indicated by the red boundary nodes in Fig. 2b. Note that $h_{d=5}(t) = h_L(t)$. The plant water uptake, S in Eq. [1], is simulated by the Feddes et al. (1978) model using the HYDRUS-3D default parameters for grass (Wesseling et al., 1991), a field-derived constant rooting depth of 0.35 m in the model domain, and an assumed uniform root activity.

We tested the transient model for two time intervals of 162 and 67 d. The first simulation was used for model calibration, started from 11 Apr. 2006, and is subsequently referred to as the TSp1 run. The second simulation was used for model evaluation, was conducted for the time period 21 June to 27 Aug. 2008, and is subsequently referred to as the TSp2 run. The initial conditions were assumed to be uniform in the x - y plane of the model domain as described by Eq. [5]. The initial pressure heads in the z direction were derived from linear interpolation of measurements. These initial pressure head measurements for the TSp1 and TSp2

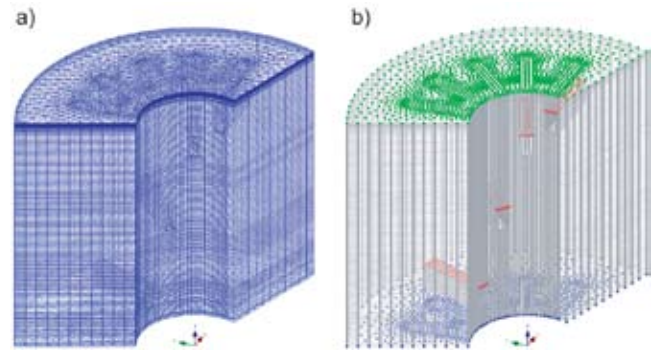


FIG. 2. Transient HYDRUS-3D vadose zone sampler model: (a) finite-element calculation mesh and (b) boundary conditions of the transient Spydia model. The green, red, and blue boundary nodes correspond to the atmospheric boundary condition at the atmosphere-soil interface, the specified head boundaries at the automated equilibrium tension lysimeters, and the specified head boundary at the bottom boundary, respectively.

runs were -0.41 and -0.87 , -1.35 and -1.21 , -1.18 and -1.12 , -0.85 and -1.00 , and -0.44 and -0.96 m at the 0.4-, 1.0-, 2.6-, 4.2-, and 5.1-m depths, respectively.

Inverse Parameter Estimation

The MVG soil hydraulic model used in this study requires the estimation of different parameters to quantify the soil water retention and unsaturated soil hydraulic conductivity functions. These parameters were taken from the soil catalog implemented in HYDRUS (sand and loam) and from Mertens et al. (2005) (ignimbrite) for the homogeneous models (Table 1). The parameters for the five-layer Spydia model were estimated using inverse modeling by minimizing the difference between the observed and modeled tensiometric pressure heads at four different observation depths. In an extension of our previous work (Wöhling et al., 2008; Wöhling and Vrugt, 2008), we set up a five-layer HYDRUS-1D model with the individual depths listed in Table 1. The initial and boundary conditions were set up in accordance with the transient-flow model described above. We used a multiobjective formulation of the parameter optimization problem utilizing four different criteria:

$$\min F(\mathbf{u}) = \begin{bmatrix} F_1(\mathbf{u}) \\ F_2(\mathbf{u}) \\ F_3(\mathbf{u}) \\ F_4(\mathbf{u}) \end{bmatrix} \quad [13]$$

where F_1 to F_4 are defined as the RMSE (e.g., Hall 2001) of the fit between the simulated and observed pressure heads at the 0.4-, 1.0-, 2.6-, and 4.2-m depths in the vadose zone profile, and \mathbf{u} is a vector of 25 MVG model parameters to be optimized (5 layers \times 5 hydraulic parameters each). The inverse problem expressed in Eq. [13] was solved with the AMALGAM evolutionary search algorithm (Vrugt and Robinson, 2007). To create the initial sample (population size $s = 100$) to be iteratively improved with AMALGAM, we used uniform sampling within the parameter bounds specified as follows: $\theta_s = 0.3$ to 0.7 m³ m⁻³, $\alpha = 1$ to 20 m⁻¹, $n = 1.1$ to 9.0 , $K_s = 10^{-7}$ to 10^{-3} m s⁻¹, and $l = 0.1$ to 1.0 . We further assumed $\theta_r = 0$. The individual optimization runs were set up for a 162-d calibration period beginning on 11

Apr. 2006 and a 10-d “spin-up” period was considered for the calculation of the performance measures. Consistent with our earlier approach, we isolated a balanced solution from the resulting Pareto surface (for the Pareto concept, see Gupta et al., 1998; Deb, 2001; Vrugt et al., 2003), i.e., the solution where the overall RMSE of all four objectives is at its minimum. This solution is subsequently referred to as the compromise solution. The HYDRUS-1D model was evaluated using independent data from the 67-d time period. The hydraulic parameters of the one-dimensional model compromise solution were then used in our HYDRUS-3D calculations for the five-layer Spydia model. Note that the multiobjective approach was used for another aspect of our work, which is not reported here, and a single-objective calibration would have been sufficient to isolate the compromise solution. We acknowledge the uncertainty in the parameter estimates but have neglected it here for the sake of clarity in our methodology and for length issues. Detailed information on our calibration method, the AMALGAM algorithm, and its parameterization has been reported in Wöhling et al. (2008) and Wöhling and Vrugt (2008) and is therefore not repeated here.

The HYDRUS-1D and HYDRUS-3D simulations of transient pressure heads were compared with each other and with the field data. We investigated whether the one-dimensional model was sufficient to calibrate the Spydia model and to accurately describe the water flow in the “undisturbed” Spydia vadose zone. The misfit between simulated HYDRUS-1D and -3D pressure heads and the observed pressure heads was evaluated using the RMSE, the coefficient of determination R^2 , and the Nash–Sutcliffe coefficient of efficiency, C_e (ASCE Task Committee on Definition of Watershed Models of the Watershed Management Committee, Irrigation and Drainage Division, 1993), a widely used fitting criterion that may assume a negative value if the mean square error of the best prediction exceeds the variance of the observations (Hall, 2001). Model predictions were considered satisfactory if the values of R^2 and C_e were close to unity.

Results and Discussion

Calibration of the Five-Layer Spydia Model

The results of the calibration and evaluation of the five-layer HYDRUS-1D model of the Spydia vadose zone sampler are summarized in Table 2 and Fig. 3 and 4. The MVG soil hydraulic model

TABLE 2. Measures of fit between the observed and simulated pressure heads at the 0.4-, 1.0-, 2.6-, and 4.2-m depths using the compromise solution parameter set in the simulation with the five-layer HYDRUS-1D model. The criteria were calculated for both the calibration and the evaluation periods.

Model depth m	Calibration period			Evaluation period		
	RMSE	R^2	C_e †	RMSE	R^2	C_e
0.4	0.072	0.93	0.93	0.115	0.92	0.60
1.0	0.057	0.95	0.95	0.066	0.90	0.89
2.6	0.081	0.85	0.85	0.170	0.89	0.78
4.2	0.040	0.93	0.93	0.080	0.97	0.93

† Nash–Sutcliffe coefficient of efficiency.

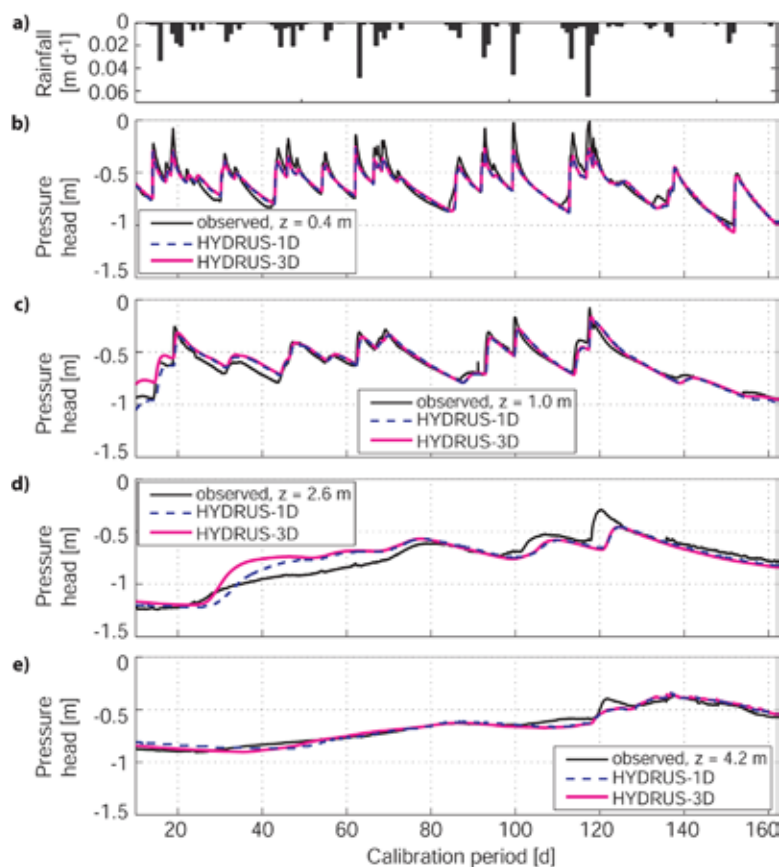


FIG. 3. Pressure head predictions of the five-layer HYDRUS-1D model for the calibration period: (a) daily rainfall, and the simulated pressure heads at the (b) 0.4-, (c) 1.0-, (d) 2.6-, and (e) 4.2-m depths. Also shown are the simulated pressure heads of the HYDRUS-3D model of the Spydia site.

parameters of the five-layer HYDRUS-1D model were estimated by the AMALGAM algorithm using observations of tensiometric pressure heads at the 0.4-, 1.0-, 2.6-, and 4.2-m depths in the Spydia vadose zone during the calibration period. The AMALGAM run was terminated after 50,000 HYDRUS-1D evaluations. One drawback of inverse modeling for vadose zone problems is the large computational requirements. For instance, one sequential optimization run required several days using the Matlab R2008a (64-bit) Microsoft Windows XP Professional (64-bit) modeling environment on a Dell Precision 390 workstation with a Quad-Core Intel Core 2 Extreme processor QX6700 (2.67 GHz) and 4 Gb of RAM. We could significantly reduce the time needed for calibration to less than one-third by parallelizing the AMALGAM code with the Matlab Parallel Computing Toolbox. Inverse parameter estimation using the HYDRUS-3D Spydia model is to date clearly not feasible, however, since the run time of a single HYDRUS-3D simulation on our workstation was 8.2 d for a 162-d simulation period. In comparison, a corresponding HYDRUS-1D run required only 20 to 30 s, which made it suitable for the large number of simulations needed in the global optimization context.

To illustrate the outcome of the calibration of the five-layer model, consider Fig. 3, which presents the simulated and observed pressure heads at the 0.4-, 1.0-, 2.6-, and 4.2-m depths using the compromise solution parameter set of

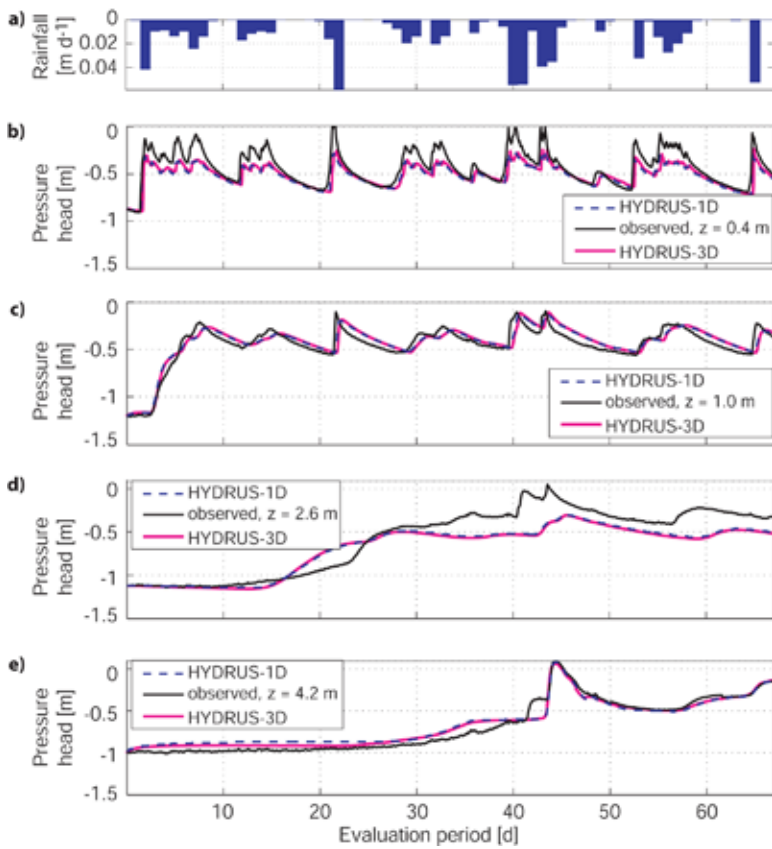


FIG. 4. Pressure head predictions of the five-layer HYDRUS-1D model for the evaluation period: (a) daily rainfall, and the simulated pressure heads at the (b) 0.4-, (c) 1.0-, (d) 2.6-, and (e) 4.2-m depths. Also shown are the simulated pressure heads of the HYDRUS-3D model of the Spydia site.

the Pareto space as calculated by AMALGAM. Table 2 summarizes the performance criteria calculated for the model calibration. The model fit the data well at the individual depths, which is confirmed by relatively small RMSE values that range between 0.040 and 0.081 m, and R^2 and C_c values >0.85 (Table 2).

The calibrated model was evaluated for a 67-d time period with independent data not previously used in the calibration. Figure 4 shows the pressure head predictions of the five-layer HYDRUS-1D model for the evaluation period. The simulated pressure heads agreed well with the data; however, the model-to-measurement misfit is larger for the evaluation period than the calibration period, which is confirmed by larger RMSE values and smaller R^2 and C_c values (Table 2). The simulated pressure

heads followed the dynamics of the observations at the 0.4-m depth, but underestimated the low-tension peaks caused by infiltration after rainfall events (Fig. 4b). This explains the lesser model fit compared with the calibration period. The observed range and dynamics of both pressure heads at the 0.4-m depth and rainfall intensity during the calibration and evaluation periods are similar, however, and thus we would expect a similar model response and performance. The difference can be attributed to a number of reasons such as the non-uniqueness of the model parameterization, inadequacy of the model structure, the large number of calibration parameters, the difference in the information content of the calibration and evaluation data, and the formulation of the objective function, as well as to physical reasons such as the seasonal change in soil hydraulic properties. In the context of our study, parameter uniqueness was previously investigated by Wöhling et al. (2008) and model structural uncertainty was analyzed using model ensemble forecasts by Wöhling and Vrugi (2008). Both studies also showed a deterioration of the model fit during the evaluation periods. Ongoing research (e.g., Gupta et al., 2008) indicates that the choice of the statistical fitting criteria in model calibration may explain at least some of these findings.

The hydraulic parameters of the five layers of the compromise solution are listed in Table 1 and were subsequently used in the five-layer HYDRUS-3D model.

Steady-State Model Analysis

The simulated pressure head and flow velocity deviated from undisturbed flow conditions at the Spydia vadose zone sampler for different vadose zone materials.

The results are summarized in Table 3 and Fig. 5 to 8. Figure 5 shows exemplarily for the ignimbrite material the simulated steady-state pressure heads for vertical cross-sections (Sections A in Fig. 1c) along the axis of the individual AETLs of the $SIg^{(d)}$ run. The left and right bounds of the x axis in each panel correspond to the caisson wall ($r = 1.15$ m) and the radial distance $r = 3.0$ m, respectively. The white rectangles in the individual panels of Fig. 5 indicate the AETL locations. The steady-state pressure head for undisturbed conditions (i.e., no flow impediments, no internal sinks in the flow domain), h_u , is specific to the hydraulic properties of the vadose zone materials. For the $SIg^{(d)}$ run, h_u equates to -1.17 m. The smallest pressure head values in the domain were -1.34 m and occurred in the dry zone

TABLE 3. Summary statistics of the steady-state simulation runs: pressure head for undisturbed flow conditions, h_u , maximum pressure head deviation from h_u at the various reference tensiometer locations, $\Delta h_{c,max}$, maximum flow velocity deviation at these locations, $\Delta v_{c,max}$, their respective mean values, and minimum and mean sampling efficiency, E_{min} and \bar{E} . Maximum values are indicated in italics.

Run	h_u	$\Delta h_{c,max}$	$\overline{\Delta h_c}$	$\Delta v_{c,max}$	$\overline{\Delta v_c}$	E_{min}	\bar{E}
	m			mm d ⁻¹			
SSa ^(d) (sand, 1 mm d ⁻¹)	-0.265	0.007	0.002	0.103	0.026	0.90	0.97
SLo ^(d) (loam, 1 mm d ⁻¹)	-0.855	0.032	0.016	0.070	0.035	0.93	0.96
SIg ^(d) (ignimbrite, 1 mm d ⁻¹)	-1.165	0.037	0.019	0.062	0.035	0.94	0.97
SSa ^(w) (sand, 3 mm d ⁻¹)	-0.224	0.004	0.001	0.270	0.058	0.91	0.98
SLo ^(w) (loam, 3 mm d ⁻¹)	-0.585	0.020	0.009	0.260	0.132	0.91	0.96
SIg ^(w) (ignimbrite, 3 mm d ⁻¹)	-0.807	0.036	0.019	0.190	0.100	0.94	0.97
SSp ^(d) (Spydia materials, 1 mm d ⁻¹)	-	0.029	0.012	0.080	0.039	0.92	0.96
SSp ^(w) (Spydia materials, 3 mm d ⁻¹)	-	0.023	0.008	0.240	0.052	0.92	0.98

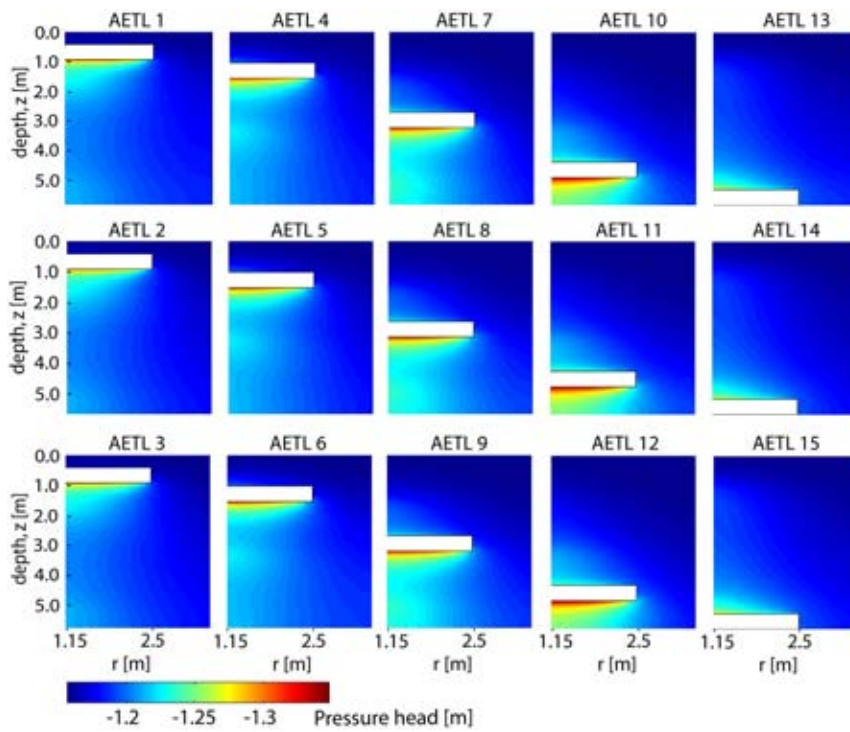


Fig. 5. Steady-state pressure heads for vertical cross-section along the axis of the individual automated equilibrium tension lysimeters (AETLs) of the dry ignimbrite run. The white boxes indicate the locations of the AETLs.

immediately under the AETLs (as indicated by the red colors in Fig. 5). Comparatively small dry zones develop also at the top of lysimeters that are installed below the 0.4-m depth. These zones increase with depth and are caused by the formulation of the boundary condition (Eq. [7]). Since the AETLs extract water from the model domain, the tensions at the reference locations progressively increase but slightly with depth with respect to h_u . Thus slightly too much water is extracted by the AETL. Since the effects are much smaller than the dry zones below the lysimeters, they were neglected here. It should be noted that the formulation of the boundary condition Eq. [7] exacerbates the dry-zone effects rather than underestimating it. In the transient scenarios described below, we correctly simulated the control of the AETLs at the individual depths corresponding to the transient pressure head at the respective reference locations.

By analyzing the vertical cross-sections for all steady-state runs, we made the following observations, which are true not only for the $SIg^{(d)}$ run but can be generalized for all the investigated runs with homogeneous materials. First, the extent of the dry zone under the AETLs increases with increasing depth. Second, the dry zone decreases with increasing distance from the caisson wall.

To further illustrate these observations, consider Fig. 6, which shows the steady-state flow velocity field of the $SIg^{(d)}$ run for vertical cylindrical cross-sections along the circumference of a circle with $r = 1.5, 2.0,$ and 2.5 m (Sections R in Fig. 1c). The undisturbed steady-state flow velocity, v_c , is 1 mm d^{-1} for the $SIg^{(d)}$ run. As seen in Fig. 6a through 6c, both the value of flow velocity divergence and the lateral extent of the dry zone decrease with distance from the caisson wall, r . The dry zones of AETLs installed deeper in the vadose zone intersect with the dry zones from AETLs installed higher up in the profile. The superposition

of the dry zones leads to consistently lower flow rates at the bottom of the flow domain ($z = 5.6$ m) compared with undisturbed flow conditions. These observations can also be generalized for all the investigated runs with the different homogeneous vadose zone materials and different boundary flux values. The flow pattern can be explained by the fact that the AETLs are acting as internal sinks and water is removed from the system by their operation. These effects are smallest at the outer distance of the AETLs ($r = 2.5$ m), as depicted in Fig. 6c. This is due to compensating diffusive flow from undisturbed areas of the vadose zone and to the greater lateral separation distance between AETLs compared with these distances closer to the access caisson. The importance of the separation distance has been discussed earlier (Mertens et al., 2005) and was considered in the design of the current layout of the Spydia experimental site.

Figure 6b depicts the cylindrical cross-section at the installation distance of the control tensiometers (as indicated by the red dots). The pressure head and flow velocity divergence from undisturbed flow conditions at the location of the control tensiometers is fundamentally linked to the sampling efficiency of the AETLs and thus to the error of flux measurements of

the Spydia vadose zone sampler. The flow velocity (and likewise the pressure heads) at these locations appear to be undisturbed at the 0.4- and 1.0-m depths. Increasing flow velocity divergence can be seen with depth (Fig. 6b). The degree of divergence varies with the type of vadose zone material, as we discuss below.

To illustrate the impact of deviations of the control pressure head from undisturbed conditions, consider Fig. 7 which shows simulated steady-state pressure heads for horizontal cross-sections (Sections B in Fig. 1c) of the $SIg^{(d)}$ run at the 0.4-, 1.0-, 2.6-, 4.2-, and 5.1-m depths. The red dots mark the tensiometer locations where the pressure head, h_c , was measured for controlling the individual AETLs. The pressure-head deviation at the control tensiometer locations, $\Delta h_c = h_u - h_c$, was zero at the 0.4-m depth and increased to values of 0.005, 0.02, 0.037, and 0.037 m at the 1.0-, 2.6-, 4.2-, and 5.1-m depths, respectively. The corresponding deviations from the undisturbed flow velocity, Δv_c , (not shown) are 0.007, 0.046, 0.080, 0.095, and 0.108 mm d^{-1} , respectively.

To compare the results of the steady-state runs utilizing different vadose zone materials, we calculated the maximum and mean deviations of pressure head and flow velocity at the five depths, $\Delta h_{c,\max}$, Δh_c , $\Delta v_{c,\max}$, and Δv_c , respectively. These statistics are summarized in Table 3. The maximum values of the individual statistics are indicated in bold. The different h_u values for each layer of the $SSp^{(d)}$ and $SSp^{(w)}$ runs are not listed. The $SIg^{(d)}$ run, which has been discussed so far, exhibits both the largest absolute ($\Delta h_{c,\max}$) and mean (Δh_c) pressure head deviations among all the runs. But this does not necessarily result in the largest flow velocity deviations. The largest absolute $\Delta v_{c,\max}$ value was 0.27 mm d^{-1} for the $SSa^{(w)}$ run. This finding cannot easily be attributed to soil texture because the $SLo^{(w)}$ run attained

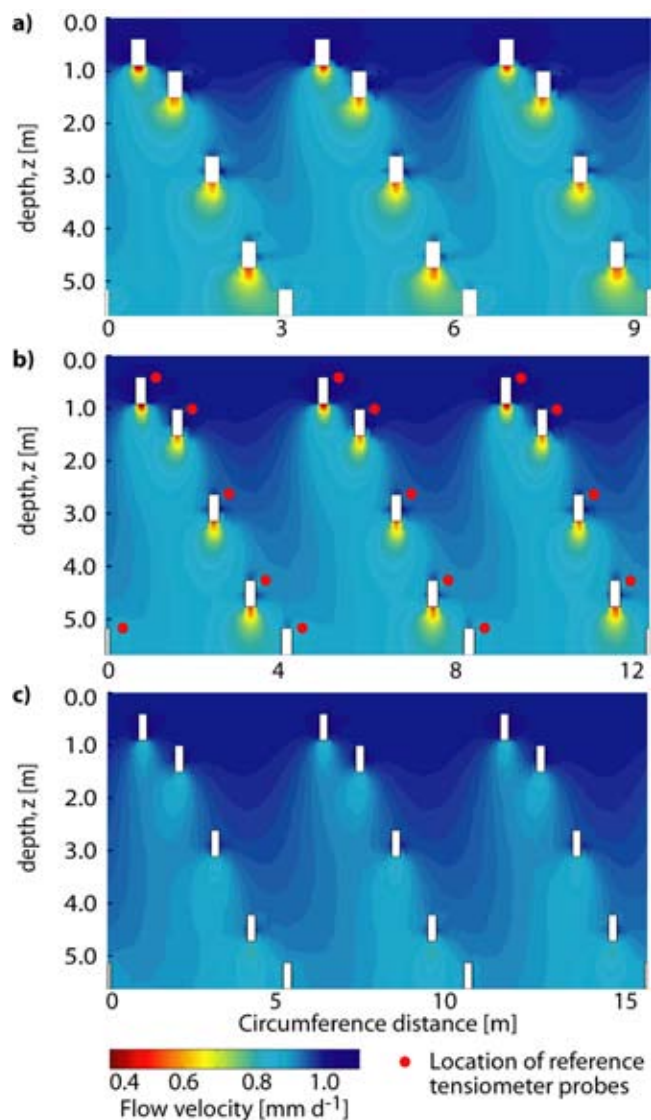


FIG. 6. Steady-state flow velocity of the dry ignimbrite run for a vertical cross-section along the circumference of the circle with (a) radius $r = 1.5$ m, (b) $r = 2.0$ m, and (c) $r = 2.5$ m. The white boxes and red dots indicate the locations of the automated equilibrium tension lysimeters and the control tensiometers, respectively.

a similar value (Table 3). Soil texture has an impact on the *extent*, however, and hence an additive effect of the dry zones as we discuss below.

Also listed in Table 3 are the minimum and mean sampling efficiency of the AETLs, E_{\min} and \bar{E} , respectively. E_{\min} attained the smallest value for the SSa^(d) run (0.90). In other words, the simulated sampling efficiency of the 15 individual AETLs at the Spydya vadose zone sampler was at least 90% for all vadose zone materials investigated. The mean sampling efficiency of the 15 AETLs combined was relatively high and varied little for the different materials at values between 96 and 98% (Table 3). This is an interesting result because soil texture apparently has less impact on the sampling efficiency than the design parameters. Interpretation of Fig. 7 demonstrates the importance of the choice of the reference location for the control tensiometer. Asymmetric flow divergence patterns develop under the AETLs by the “umbrella effect” and the tensiometers installed at the 4.2- and 5.1-m depths are very close to the boundaries of the dry

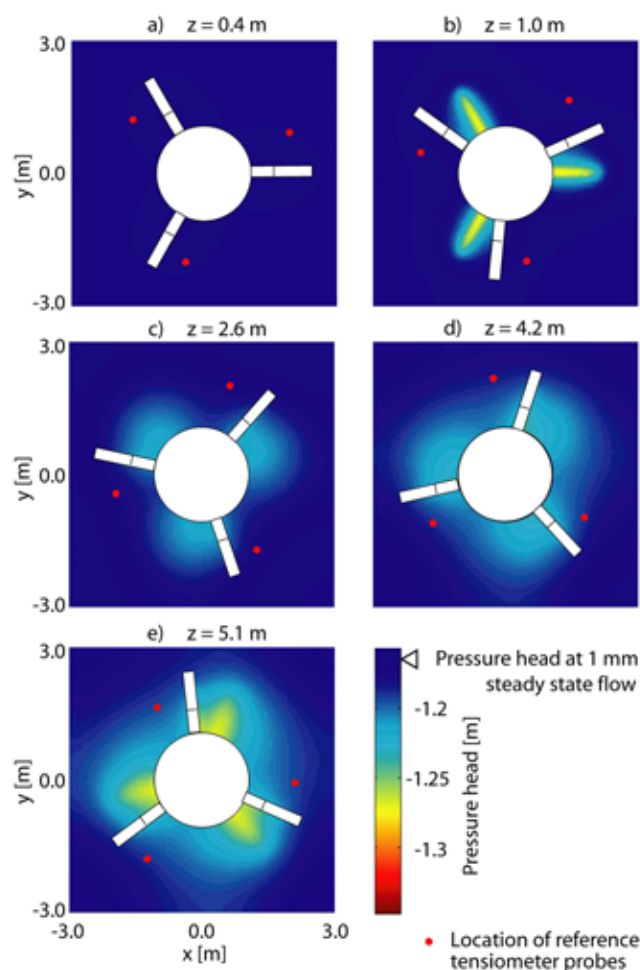


FIG. 7. Steady-state pressure heads for horizontal cross-sections of the dry ignimbrite run at the (a) 0.4-, (b) 1.0-, (c) 2.6-, (d) 4.2-, and (e) 5.1-m depths. Also indicated are the locations of the automated equilibrium tension lysimeters and the locations of the control tensiometers.

zones from the AETLs installed at the 2.6- and 4.2-m depths, respectively. This can also be seen in the flow pattern shown in the vertical section depicted in Fig. 6.

It became apparent from the analysis above that pressure-head divergences were smaller at greater radial distance from the access caisson (Fig. 6 and 7). Hence, greater sampling efficiencies of individual AETLs can be expected when shifting the control tensiometer locations “further out” to a radial distance of $r = 2.5$ m. We estimated that the sampling efficiency of the AETLs installed at the 4.2- and 5.1-m depths could increase by up to 5%. The field hydraulic properties are subject to local variability, however, and the materials at the tensiometer locations should ideally be representative of the materials above the individual AETLs. Since the local variability of the materials at the Spydya field site is unknown, this trade-off is difficult to quantify.

Revisiting Fig. 5, 6, and 7, we can see a reoccurrence of the pressure head and flow velocity patterns of the AETLs 1, 4, 7, 10, and 13 in AETLs 2, 5, 8, 11, and 14, and AETLs 3, 6, 9, 12, and 15, respectively. This is a result of their symmetrical alignment around the access caisson (c.f. Figure 1c). Therefore, we considered it sufficient to visualize the subsequent results for the sector with AETLs 1, 4, 7, 10, and 13.

We compared the flow field divergence for the different vadose zone materials, i.e., for the sand, loam, ignimbrite, and the five-layer Spydia model. Figure 8a shows the simulated flow velocity for vertical cross-sections along the circumference segment ($r = 2.0$ m) between AETL 1 and AETL 13 for the runs with 1 mm d^{-1} flux boundary condition. The dry zones developing below the AETLs had the largest extent in the sandy vadose zone, run $SSa^{(d)}$, where they affected other AETLs. The extent of the dry zone in the five-layer model and the ignimbrite materials was significantly smaller and rather more isolated than affecting other AETLs. The smallest dry zones were simulated in the loam material, run $SLo^{(d)}$. Disturbances are apparent at the boundaries between subsequent layers in the Spydia five-layer model (Fig. 8a, Panel 4 at the far right). This is caused by the method by which the calculation results were post-processed, since nodal flux is calculated as a product of nodal conductivity and the average gradient from all elements connecting the node, and pressure heads are different in different materials across a boundary for the same flux.

Figure 8b shows the simulated flow velocity for the runs with a 3 mm d^{-1} flux boundary condition. The extent of the dry zone was again largest for the sand [run $SSa^{(w)}$]. Although significantly smaller in their extent, the dry zones simulated for the loam material [run $SLo^{(w)}$] were also relatively large and affected by other AETLs with depth. Similar in shape but again slightly smaller dry zones were simulated for the $SSp^{(w)}$ run. The dry zones were again affected by other AETLs. In contrast, the effects were smallest and isolated in the ignimbrite material (Panel 3 in Fig. 8b).

These results demonstrate that the extent of the dry zones is not only dependent on the texture of the vadose zone materials but also on the flow conditions, i.e., the state of the system. This can be explained by the different unsaturated flow properties of the materials described by their soil hydraulic functions.

Transient, Three-Dimensional Spydia Model

We next compared the simulation results of the transient HYDRUS-3D Spydia model runs TSP1 and TSP2 with the corresponding HYDRUS-1D simulations and field observations. The results are summarized in Fig. 3, 4, and 9 and Tables 2 and 4. The soil hydraulic parameter set used in both the one-dimensional and three-dimensional models was estimated by inverse modeling using HYDRUS-1D and pressure heads measured at the Spydia site as described above. Table 4 lists the performance criteria for the TSP1 and TSP2 runs. The HYDRUS-3D simulations of pressure heads at the reference locations are shown in Fig. 3 and agree favorably with the observations during the calibration period, which is confirmed by small RMSE values of 0.064, 0.057, 0.106, and 0.035 m at the 0.4-, 1.0-, 2.6-, and 4.2-m depths, respectively, and relatively large R^2 and C_e values. In addition, the simulations matched closely to the HYDRUS-1D model calculations, which attained similar performance criteria at the individual depths (cf. Tables 2 and 4). The measure of misfit for the transient HYDRUS-3D model was slightly larger during the evaluation period, with RMSE values of 0.129, 0.077, 0.182, and

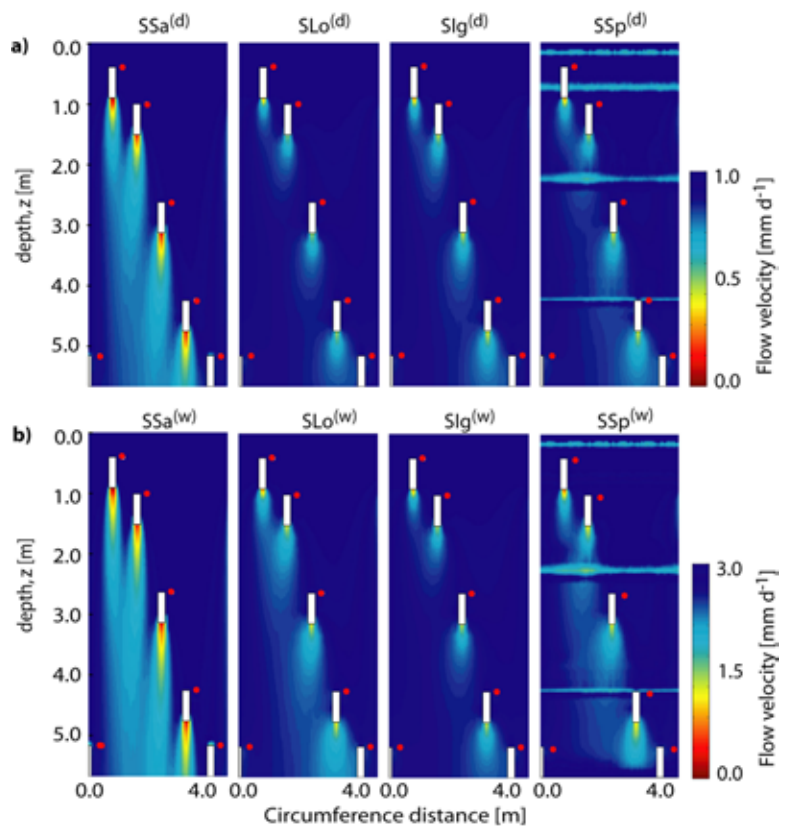


FIG. 8. Steady-state flow velocity for vertical cross-sections along the circumference of the circle with radius $r = 2.0$ m. Shown are the sections for the automated equilibrium tension lysimeters (AETLs) 1, 4, 7, 10, and 13 of (a) the dry (1 mm d^{-1}) sand [$SSa^{(d)}$], loam [$SLo^{(d)}$], ignimbrite [$SIg^{(d)}$], and Spydia [$SSp^{(d)}$] vadose zone material runs and (b) the wet (3 mm d^{-1}) sand [$SSa^{(w)}$], loam [$SLo^{(w)}$], ignimbrite [$SIg^{(w)}$], and Spydia [$SSp^{(w)}$] vadose zone material runs. The white boxes and red dots indicate the locations of the AETLs and the control tensiometers, respectively.

0.065 m for the 0.4-, 1.0-, 2.6-, and 4.2-m depths, respectively, with smaller R^2 and C_e values (Table 4). Figure 4b to 4e show the corresponding simulated pressure heads at the tensiometer locations during the evaluation period. They trace closely the one-dimensional simulations at the various depths including the underestimated low-tension peaks at the 0.4-m depth.

The evaluation data differ from the calibration data inasmuch as the water table rose about 1.5 m in the short time interval between 41 and 44 simulation days. This can be explained as a catchment response to a heavy rainfall starting at Day 40 and lasting until Day 45 rather than as a response of water moving vertically through the vadose zone profile. During this time period, the simulated flow in the lower vadose profile was significantly affected by the lower boundary condition. The tensiometric pressure head at the 4.2-m depth was steeply decreasing to values slightly above zero (water saturation) at Day 44 (Fig. 4e). The almost perfect match to the observations at this depth from Day 43 on was probably also driven by the lower boundary condition. At the beginning of the simulations, the simulated pressure heads at the 4.2-m depth were slightly lower than the corresponding one-dimensional model simulations (Fig. 4e), which is a result of water being removed from the system by the AETLs' operation. The differences diminished after simulation Day 27 of the evaluation period as the water table slowly rose. The simulated pressure

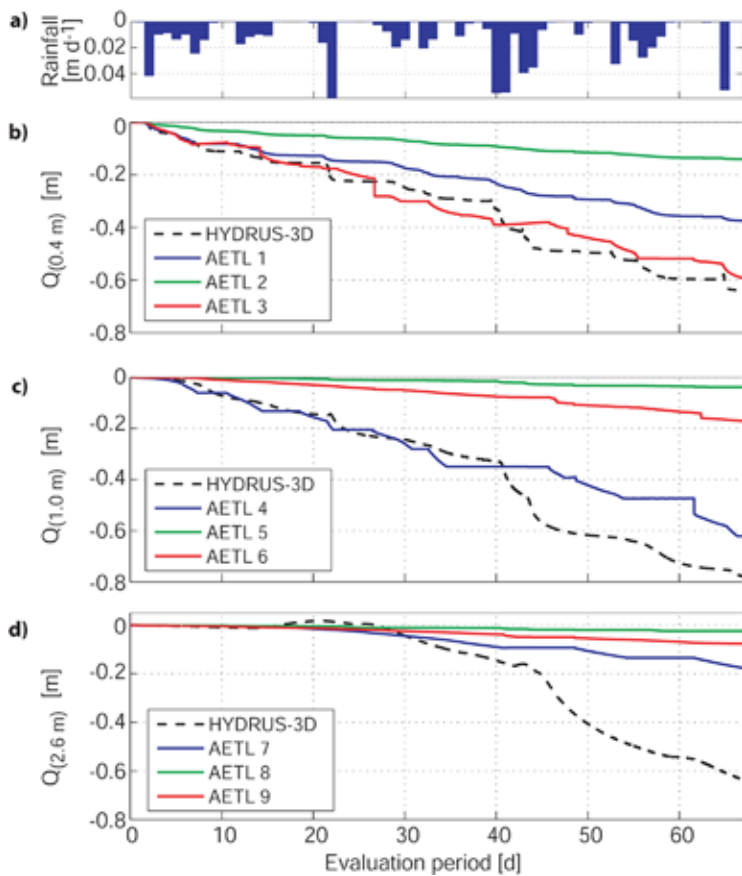


FIG. 9. Measured cumulative fluxes at automated equilibrium tension lysimeter AETL 1 to AETL 9 and the corresponding HYDRUS-3D model simulations for the evaluation period: (a) daily rainfall and the cumulative fluxes calculated for the (b) 0.4-, (c) 1.0-, and (d) 2.6-m depths.

heads at the 2.6-m depth exhibited the largest measure of misfit (Fig. 4d; Table 4), which can be related to the effects described above, possibly enhanced by model structural inadequacy. It appears that some intense rainfall events cause water to progress to larger depths rather quickly (c.f. corresponding pressure head peaks in Fig. 3 and 4). This is an indication of the occurrence of preferential flow, which cannot be modeled adequately by the uniform flow model used in this study.

Figures 9b, 9c, and 9d show the initial results of measured water fluxes during the evaluation period at the 0.4-, 1.0-, and 2.6-m depth, respectively. The fluxes at the 4.2-m depth are not included because the AETLs 10 to 13 were switched off for an extended period of time due to the rising water table. We emphasize that the measurements are “raw” data, i.e., the cumulated load cell weights. The cumulated weights were divided by the surface area of the AETL, which yields cumulative flux, Q (in $\text{m}^3 \text{m}^{-2}$ or m). The Q values appear negative when removed from the vadose zone. We did not account for possible errors of the flux measurements, which may be caused by errors in the tensiometer readings used to control the AETLs. Striking is the large spread of the cumulative flux measurements at the 0.4- and 1.0-m depths (Fig. 9b and 9c). We have yet to explore whether this spread is due to variability in the local soil hydraulic properties

or partly caused by operational control factors used in the AETLs. Therefore the results presented subsequently must be considered with care. Local soil hydraulic variability, however, is expected to be largest close to the surface and in the active root zone and the AETLs 1 to 3 were installed at the bottom of the root zone (0.4-m depth). The cumulative fluxes at the end of the evaluation period were smaller at the 2.6-m depth than the cumulative fluxes measured at the 0.4-m depth because the vadose zone profile was slowly wetting up after a dry summer. This is in agreement with the pressure head observations, which confirm the wetting front moving vertically through the profile (Fig. 4).

In our HYDRUS-3D model of the Spydia site, we assumed uniform hydraulic properties. The simulated Q values at the 0.4-m depth ($Q_{0.4\text{m}}$) are similar to the values measured at AETL 3 but the response to rainfall events was timed differently (Fig. 9b). The simulated values of $Q_{1.0\text{m}}$ matched with AETL 4 until Day 40 of the evaluation period but were larger afterward. This was probably caused by times when AETL 4 was nonoperational. During simulation Days 18 and 28, the boundary condition applied at the AETL at the 2.6-m depth forced water to enter the model domain (Fig. 9d). This is an artifact with little impact. More importantly, the simulated cumulative flux, $Q_{2.6\text{m}}$, is three times larger than the cumulative flux measured in AETL 7. We have already noted that the 2.6-m depth is the depth with the largest measure of misfit for pressure-head predictions; however, our results show a large difference between the ranges of observed and simulated cumulative fluxes. The differences can partly be attributed to the occurrence of preferential flow in the vadose zone and the inadequacy of the uniform flow model used in the study to describe this process. Another part could be related to the spatial variability of the soil hydraulic properties. The saturated conductivity determined in the laboratory from small-scale vadose zone samples varied significantly, as reported in Wöhling et al. (2008), but the in situ spatial heterogeneity is to date not well understood. It may, however, affect the accuracy of the flux measurements with a specific AETL if the characteristics at the location of the reference tensiometer are significantly different from the average soil hydraulic properties above the lysimeter. A much smaller contribution to the differences between simulated and measured fluxes can also arise from the operation of individual AETLs being interrupted for small maintenance and adjustment time periods as the measurement system is under ongoing development. The aforementioned factors together can to some extent explain the variability of the measurements.

TABLE 4. Measures of fit between the observed and calculated pressure heads at the 0.4-, 1.0-, 2.6-, and 4.2-m depths for the transient HYDRUS-3D simulations for the calibration and evaluation periods.

Model depth	Calibration period			Evaluation period		
	RMSE	R^2	C_e †	RMSE	R^2	C_e
	m			m		
0.4	0.064	0.91	0.88	0.129	0.75	0.49
1.0	0.057	0.90	0.89	0.077	0.86	0.86
2.6	0.106	0.79	0.78	0.182	0.87	0.76
4.2	0.035	0.96	0.95	0.065	0.97	0.95

† Nash–Sutcliffe coefficient of efficiency.

The magnitude of the discrepancies between simulated and measured fluxes can be affected by the information content and type of the calibration data. It can be shown that calibrating the model with one data type and evaluating the model with another data type can lead to large errors in the evaluated (predicted) quantity (Wöhling, 2009). By calibrating the model with pressure-head data, it is informed only about one variable of the water retention function, $\theta(h)$, which can result in considerable uncertainty of the other variable, i.e., the volumetric water content. It can be further shown that a relatively large range of water retention functions calibrate the model equally well (Wöhling, 2009). A part of the model discrepancies may therefore be attributed to the insufficient representation of the unsaturated flow by the Richards equation but also to the inaccuracy of the estimated water retention and unsaturated conductivity functions when their parameters are fitted to (averaged) pressure-head data. This topic is the subject of another study currently being conducted.

Summary and Conclusions

We developed a three-dimensional HYDRUS-3D model for the Spydia vadose zone sampler and investigated the pressure head and flow divergences from undisturbed flow conditions caused by the design and operation of the experimental setup. In all our model runs, we found that the dry zones developing under the individual AETLs were increasing in extent with increasing depth below the ground surface. They were, however, consistently decreasing with increasing radial distance from the center point of the access caisson plane due to the greater lateral separation distances between the horizontal projections of the AETLs. The accuracy of the tensiometric pressure head measurement adjacent to the AETLs is crucial for the accurate operation of the lysimeters. Pressure-head deviations at these reference locations lead inevitably to errors in the flux measurements. The largest pressure-head deviations from steady-state conditions at the reference locations were relatively small at 0.037 m for the ignimbrite material. The largest absolute flow divergence occurred in the sand (0.27 mm d^{-1}), notably in conjunction with the lowest pressure-head differences (0.004 m); however, the extent of the dry zones below the AETLs was also largest in the sand. In addition, the zones merged at depth in the sand whereas they stayed isolated in most other materials. The minimum and mean sampling efficiency of the AETLs varied little between the different materials under investigation and attained values greater than 0.90 and 0.96, respectively. Our analysis of the simulated three-dimensional pressure head fields revealed that the sampling efficiency of the AETLs installed at the 4.2- and 5.1-m depths could be increased by shifting the tensiometer reference location from its current position to a greater radial distance from the access caisson. The design of the Spydia vadose zone sampler presented in this study appears to be suitable for a range of different materials. We highly recommend three-dimensional flow modeling before installation at a particular field site, however, to optimize design features such as the horizontal and vertical separation distances of the AETLs.

The pressure heads simulated with the equally weighted parameter solution of the one-dimensional model calibration matched well to the measured pressure heads at the different depths in the vadose zone. The set of hydraulic parameters was then used in transient HYDRUS-3D simulations for two different

time periods using data from the Spydia site. The simulated pressure heads of the three-dimensional model matched closely to the pressure heads of the one-dimensional model and thus similarly well to the observations. This result suggests that one-dimensional modeling is well suited to calibrate the hydraulic properties of what we assume are undisturbed flow conditions. But it is not a substitute for analyzing the complex three-dimensional flow patterns developing around the Spydia vadose zone sampler under transient conditions.

We compared the “raw” data of measured cumulative AETL fluxes to the simulated cumulative fluxes. The cumulative fluxes at the three AETLs installed at each depth exhibited a large spread. We are confident, however, that the measurements are more accurate than fixed-tension flux measurement methods. The spread of the measurements reflect vadose zone characteristics such as preferential flow paths and the spatial variability of soil hydraulic properties that are not considered in the model or lumped by the calibrated model parameters. The HYDRUS-3D simulated cumulative fluxes were larger than the measurements during a 67-d evaluation period. We suggest that a significant part of the discrepancy can be attributed to the insufficient representation of the unsaturated flow by the Richards equation and to the non-uniqueness of the estimated water retention and unsaturated conductivity functions when the model parameters are calibrated on pressure-head data.

ACKNOWLEDGMENTS

This work is funded by the New Zealand International Science and Technology Linkages Fund (ISAT), the International Bureau of the German Federal Ministry of Education and Research (BMBF), and the New Zealand Foundation for Research, Science and Technology (FRST).

References

- Allen, R.G., L.S. Pereira, D. Raes, and M. Smith. 1998. Crop evapotranspiration. FAO Irrig. Drain. Pap. 56. FAO, Rome.
- ASCE Task Committee on Definition of Watershed Models of the Watershed Management Committee, Irrigation and Drainage Division. 1993. Criteria for evaluation of watershed models. *J. Irrig. and Drain. Div.* 119:429–442.
- Brye, K., J. Norman, L. Bundy, and S. Gower. 1999. An equilibrium tension lysimeter for measuring drainage through soil. *Soil Sci. Soc. Am. J.* 63:536–543.
- Celia, M.A., E.T. Bouloutas, and R.L. Zarba. 1990. A general mass-conservative numerical solution for the unsaturated flow equation. *Water Resour. Res.* 26:1483–1496.
- Deb, K. 2001. Multi-objective optimization using evolutionary algorithms. John Wiley & Sons, Chichester, UK.
- Dorrance, D.W., L.G. Wilson, L.G. Everett, and S.J. Cullen. 1991. Groundwater residue. ACS Symp. Ser. 465:300–331.
- Feddes, R.A., P. Kowalik, and H. Zaradny. 1978. Simulation of field water use and crop yield. PUDOC, Wageningen, the Netherlands.
- Gupta, H.V., S. Sorooshian, and P.O. Yapo. 1998. Toward improved calibration of hydrologic models: Multiple and noncommensurable measures of information. *Water Resour. Res.* 34:751–764.
- Gupta, H.V., T. Wagener, and Y. Liu. 2008. Reconciling theory with observations: Elements of a diagnostic approach to model evaluation. *Hydrol. Processes* 22:3802–3813.
- Hall, J.M. 2001. How well does your model fit the data? *J. Hydroinformatics* 3:49–55.
- Kosugi, K., and M. Katsuyama. 2004. Controlled-suction period lysimeter for measuring vertical water flux and convective chemical fluxes. *Soil Sci. Soc. Am. J.* 68:371–382.
- Masarik, K., J. Norman, K. Brye, and J. Baker. 2004. Improvements to measuring water flux in the vadose zone. *J. Environ. Qual.* 33:1152–1158.
- Mertens, J., G.F. Barkle, and R. Stenger. 2005. Numerical analysis to investigate

- the effects of the design and installation of equilibrium tension plate lysimeters on leachate volume. *Vadose Zone J.* 4:488–499.
- Mertens, J., J. Diels, J. Feyen, and J. Vanderborght. 2007. Numerical analysis of passive capillary wick samplers prior to field installation. *Soil Sci. Soc. Am. J.* 71:35–42.
- Mualem, Y. 1976. A new model for predicting the hydraulic conductivity of unsaturated porous media. *Water Resour. Res.* 12:513–522.
- van Genuchten, M.Th. 1980. A closed-form equation for predicting the hydraulic conductivity of unsaturated soils. *Soil Sci. Soc. Am. J.* 44:892–898.
- Vrugt, J.A., H.V. Gupta, L.A. Bastidas, W. Bouten, and S. Sorooshian. 2003. Effective and efficient algorithm for multiobjective optimization of hydrologic models. *Water Resour. Res.* 39(8):1214, doi:10.1029/2002WR001746.
- Vrugt, J.A., and B.A. Robinson. 2007. Improved evolutionary optimization from genetically adaptive multimethod search. *Proc. Natl. Acad. Sci.* 104:708–711.
- Šimůnek, J., M.Th. van Genuchten, and M. Šejna. 2006. The HYDRUS software package for simulating the two- and three-dimensional movement of water, heat, and multiple solutes in variably-saturated media. Technical manual. PC Progress, Prague, Czech Republic.
- Weiherrmüller, L., R. Kasteel, J. Vanderborght, T. Pütz, and H. Vereecken. 2005. Soil water extraction with suction cup: Results of numerical analysis. *Vadose Zone J.* 4:899–907.
- Wesseling, J.G., J.A. Elbers, P. Kabat, and B.J. van den Broek. 1991. SWATRE: Instructions for input. Internal note. Winand Staring Centre, Wageningen, the Netherlands.
- Wilson, L.G., D.W. Dorrance, W.R. Bond, L.G. Everett, and S. Cullen. 1995. In situ pore-liquid sampling in the vadose zone. p. 477–521. *In* L.G. Wilson et al. (ed.) *Handbook of vadose zone characterization and monitoring*. CRC Press, Boca Raton, FL.
- Wöhling, Th. 2009. Does vadose zone forecasting depend on the type of calibration data? p. 2377–2383. *In* R.S. Anderssen et al. (ed.) *Proc. World IMACS Congr. and MODSIM09 Int. Congr. on Modell. and Simul.*, 18th, Cairns, Australia. 13–17 July 2009. *Modell. Simul. Soc. Aust. N.Z.*, Canberra, ACT, Australia.
- Wöhling, Th., and J.A. Vrugt. 2008. Combining multi-objective optimization and Bayesian model averaging to calibrate forecast ensembles of soil hydraulic models. *Water Resour. Res.* 44:W12432, doi:10.1029/2008WR007154.
- Wöhling, Th., J.A. Vrugt, and G.F. Barkle. 2008. Comparison of three multiobjective algorithms for inverse modeling of vadose zone hydraulic properties. *Soil Sci. Soc. Am. J.* 72:305–319.